11
Sampling calorimeters

A device that measures the total energy deposited by a particle or group of particles is known as a calorimeter, in analogy with the laboratory instrument that measures the amount of deposited heat. We have already encountered several devices, such as sodium iodide scintillation counters and total absorption Cerenkov counters, that can be used as calorimeters for photon detection. We will consider properties of these "continuous" calorimeters again in Chapter 14. In this chapter we consider a class of calorimeters that periodically sample the development of a shower initiated by an incident particle. There are two major types of sampling calorimeters, depending on whether the incident particle initiates an electromagnetic or hadronic shower. Each type of calorimeter is optimized to maximize the rejection of the other type of shower.

Calorimeters have found wide use in particle physics experiments. Neutral particles can only be detected by using this method. Sampling calorimeters of very large size have been used as neutrino detectors. We have seen that at high energy, particle multiplicities grow with increasing energy, and the angular distribution of groups of the produced secondaries are highly collimated (jet effect). Under these conditions calorimeters can provide a useful trigger for interesting events based on the total energy deposited in a localized area. Calorimeters can easily be modularized and made to cover large solid angles. In addition, we shall see that the size of a calorimeter needed to measure the energy of a particle scales like $\ln(E)$, whereas the size of a magnetic deflection device would scale like $E^{1/2}$ [1].

11.1 Electromagnetic showers

Consider an electron or positron with several GeV energy traversing a slab of some material. As far as shower development is con-

Downloaded from https://www.cambridge.org/core. UNIVERSIDAD AUTONOMA METROPOLITANA, on 15 Nov 2026 at 20:24:52, subject to the Cambridge Core terms of use, available at https://www.cambridge.org/core/terms. https://doi.org/10.1017/9781009290098.012

cerned, the electron and the positron behave almost identically, and unless stated otherwise, the discussion of electron behavior in what follows also refers to positrons. We saw in Chapter 2 that for energies above 100 MeV electrons lose energy almost entirely through bremsstrahlung. The emitted photons typically carry off a large fraction of the electron's initial energy. For photons with energy greater than 100 MeV the major interaction is pair production, which gives another energetic electron or positron. In this manner a single initial electron or photon can develop into an electromagnetic shower, consisting of many electrons and photons. The shower continues until the particles' energy falls below 100 MeV, at which point dissipative processes, such as ionization and excitation, become more important.

The mathematical description of the development of a completely general electromagnetic shower is extremely complex and cannot be solved in closed form [2]. The theory has been worked out with several simplifications. First, one only considers the average behavior of the shower, or fluctuations from the average behavior. Second, since at high energy the angles of emission of the electrons and photons are small, the shower will develop primarily in the forward direction. It is then customary to treat separately the longitudinal and transverse developments.

The unit of distance traversed is typically measured in radiation lengths, given approximately by [1]

$$X_{\text{rad}} = 180A/Z^2 \qquad \text{g/cm}^2 \tag{11.1}$$

Values of the radiation lengths of many materials were given in Table 2.1. Shower calculations usually make a number of approximations. (1) At high energy the probabilities for bremsstrahlung and pair production are assumed to be independent of Z when distances are measured in radiation lengths. (2) The theoretical cross sections are based on the Born approximation and are most reliable for low Z materials. Deviations in large Z materials are proportional to Z^2. (3) The difference in cross sections for high energy electrons and positrons is neglected. (4) The asymptotic formulas for radiation and pair production are assumed valid. (5) The Compton effect and collisional processes are neglected at high energy.

A particularly subtle point is how to handle the transition to the region where the collisional energy loss is important. Sometimes a sharp cutoff η is assumed such that whenever the energy of a shower particle falls below η, it is considered to lose the remainder of its energy to collisions. This can be taken to be the critical energy E_c from Eq. 2.54, which we recall is the collision energy loss per radiation length of an electron with energy E_c. One can also consider a constant collision loss.

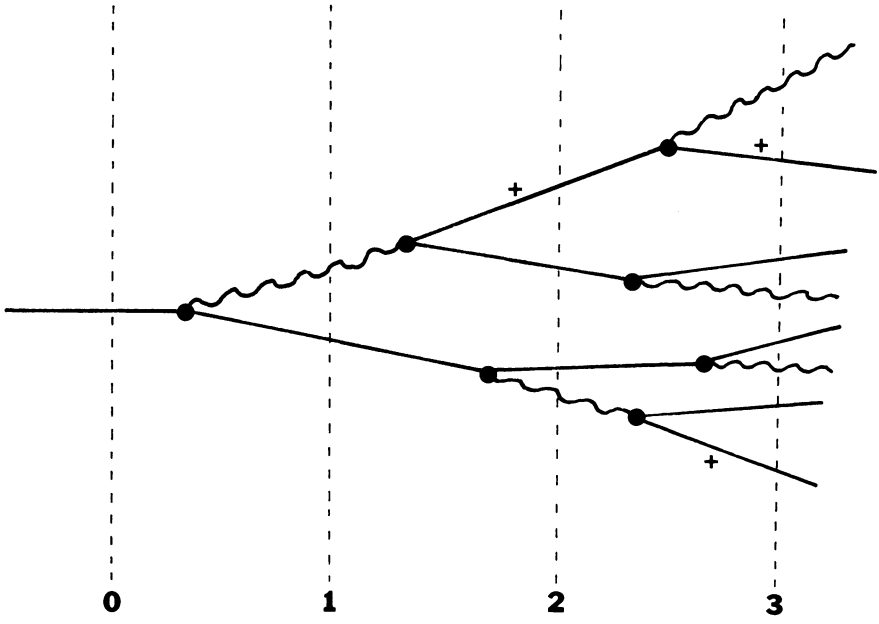
Downloaded from https://www.cambridge.org/core. UNIVERSIDAD AUTONOMA METROPOLITANA, on 15 Nov 2026 at 20:24:52, subject to the Cambridge Core terms of use, available at https://www.cambridge.org/core/terms. https://doi.org/10.1017/9781009290098.012

A simple model that gives the correct qualitative description of the longitudinal development of a shower has been given by Heitler [3]. The model makes the following assumptions. (1) Each electron with $E > E_c$ travels 1 radiation length and then gives up half its energy to a bremsstrahlung photon. (2) Each photon with $E > E_c$ travels 1 radiation length and then undergoes pair production with each created particle receiving half of the energy of the photon. (3) Electrons with $E < E_c$ cease to radiate and lose their remaining energy to collisions. (4) Neglect ionization losses for $E > E_c$.

Suppose we begin with an electron of energy $E_0 \gg E_c$, as shown in Fig. 11.1. After the first radiation length there will be one electron and one photon, each with energy $E_0/2$. In the second radiation length the electron emits a second photon, while the first photon undergoes pair production into an electron–positron pair. Thus, after 2 radiation lengths there will be two electrons, one positron, and one photon in the shower, each with energy $E_0/4$.

This simple model predicts a number of features of electromagnetic showers. (1) In the development of the shower the total number of parti-

Figure 11.1 Simple model for the development of an electromagnetic shower. Solid lines (with +) indicate electrons (positrons) and wavy lines indicate photons. The numbers at the bottom show the distance measured in radiation lengths.



Downloaded from https://www.cambridge.org/core. UNIVERSIDAD AUTONOMA METROPOLITANA, on 15 Nov 2026 at 20:24:52, subject to the Cambridge Core terms of use, available at https://www.cambridge.org/core/terms. https://doi.org/10.1017/9781009290098.012

cles present after t radiation lengths is

$$N(t) = 2^t = e^{t \ln 2} \tag{11.2}$$

Thus, the number of shower particles increases exponentially with t. (2) There will be approximately equal numbers of electrons, positrons, and photons in the shower. (3) The average energy of a shower particle at the depth t is

$$E(t) = E_0/2^t \tag{11.3}$$

(4) The depth at which the shower energy equals some value E' occurs when $E(t) = E'$, and

$$t(E') = \frac{\ln(E_0/E')}{\ln 2} \tag{11.4}$$

(5) The shower has the maximum number of particles when $E(t) = E_c$. This occurs at the depth

$$t_{max} = \frac{\ln(E_0/E_c)}{\ln 2} \tag{11.5}$$

At this point the shower abruptly stops. Note that the maximum shower depth increases logarithmically with primary energy. (6) The number of particles at the maximum is

$$N_{max} = e^{t_{max} \ln 2} = E_0/E_c \tag{11.6}$$

Thus, the maximum number of shower particles is directly proportional to the incident energy. (7) The number of particles in the shower that have energy greater than some value E' is ($E' \ll E_0$)

$$\begin{aligned} N(E > E') &= \int_0^{t(E')} N(t)\, dt \\ &\simeq \frac{1}{\ln 2} \frac{E_0}{E'} \end{aligned} \tag{11.7}$$

Thus, the energy spectrum dN/dE' falls like $1/E'^2$. (8) The sum of all the track lengths of all charged particles in the shower is

$$\begin{aligned} L &= \frac{2}{3} \int_0^{t_{max}} N(t)\, dt \\ &\simeq \frac{E_0}{E_c} \end{aligned} \tag{11.8}$$

We see that the total charged track length is directly proportional to the incident energy.

The discontinuous behavior at t_{max} is the result of the overly simplified assumptions. Quantitatively accurate treatments of shower development are generally performed using Monte Carlo techniques. These calcula-

Downloaded from https://www.cambridge.org/core. UNIVERSIDAD AUTONOMA METROPOLITANA, on 15 Nov 2026 at 20:24:52, subject to the Cambridge Core terms of use, available at https://www.cambridge.org/core/terms. https://doi.org/10.1017/9781009290098.012

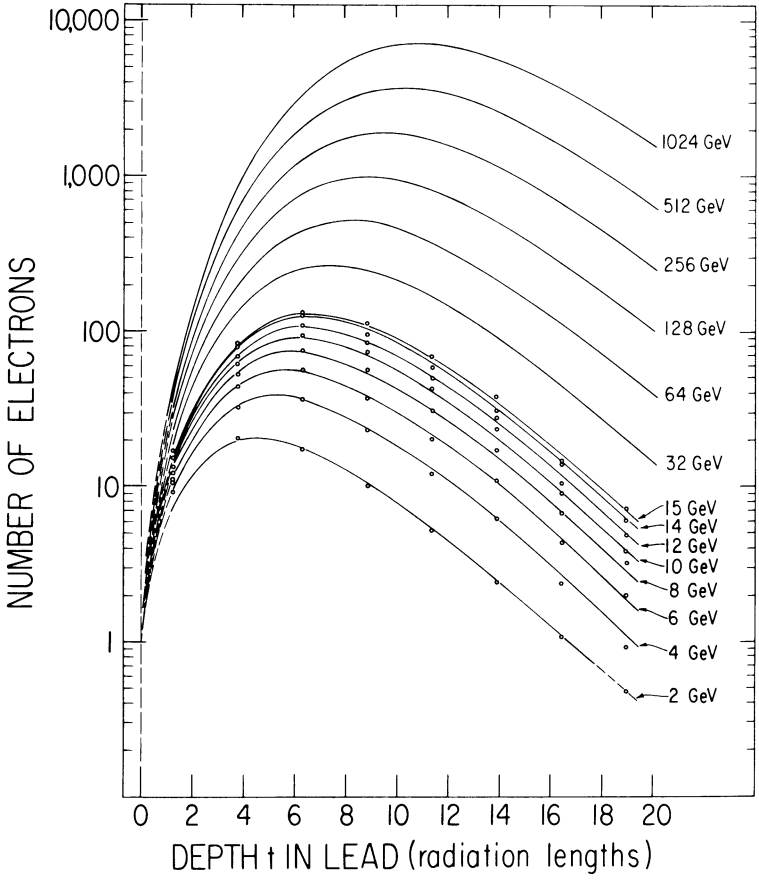
tions can take into account the energy dependence of the cross section, the lateral spread of the shower due to multiple scattering, statistical fluctuations, and other complications.

Shower data for the number of particles with energy greater than E' as a function of depth in the shower is shown in Fig. 11.2, along with the results of more accurate calculations. We see that the discontinuity at t_{max} has been broadened into a long tail. The data [4] indicate that the following empirical formulas are accurate from 2 to 300 GeV. The maximum number of electrons occur at the depth

$$t_{max} = 3.9 + \ln E_0 \tag{11.9}$$

where t_{max} is measured in radiation lengths and E_0 is in GeV. The number

Figure 11.2 Shower profiles in lead. The number of electrons should be multiplied by a normalization factor of 0.79. (D. Müller, Phys. Rev. D 5: 2677, 1972.)



Downloaded from https://www.cambridge.org/core. UNIVERSIDAD AUTONOMA METROPOLITANA, on 15 Nov 2026 at 20:24:52, subject to the Cambridge Core terms of use, available at https://www.cambridge.org/core/terms. https://doi.org/10.1017/9781009290098.012

of electrons at the maximum is given by

$$N_{\max} = 8.46E_0^{0.935} \tag{11.10}$$

Let $N(E_0, t)$ be the number of shower electrons at depth t resulting from a particle of energy E_0. The total path length of electrons in the shower is

$$\begin{aligned} L(E_0) &= \int_0^\infty N(E_0, t)\, dt \\ &= 60.2E_0 \end{aligned} \tag{11.11}$$

The energy dependence of the last three equations are in qualitative agreement with the simple model (Eqs. 11.5, 11.6, and 11.8).

The longitudinal development of electromagnetic showers in different materials is found to scale if distances are measured in radiation lengths [1]. Figure 11.3 shows showers created by 6-GeV/c electrons in aluminum, copper, and lead. The scaling is seen to hold rather accurately over the first 15 radiation lengths. Also shown is the shower radius at each depth that contains 90% of the shower particles. Up to the shower maximum the shower is contained in a cylinder with radius < 1 radiation length. Beyond that point the electrons are increasingly affected by multiple scattering, and the lateral size scales in the "Moliere radius," which is given approximately as [1]

$$\rho_m \simeq 7A/Z \qquad \text{g/cm}^2 \tag{11.12}$$

The propagation of photons in the shower causes deviations from Moliere radius scaling [5]. However, roughly 95% of the shower is contained laterally in a cylinder with radius $2\rho_m$.

The number of shower tracks found inside a ring of radius r at the depth of the shower maximum is found to increase as a power of the variable rE_0, where E_0 is the energy of the electron initiating the shower [6]. The result is independent of E_0 over the range 50 – 300 GeV. This implies that a cylinder containing a fixed number of shower particles is found closer and closer to the shower axis as the incident energy is increased.

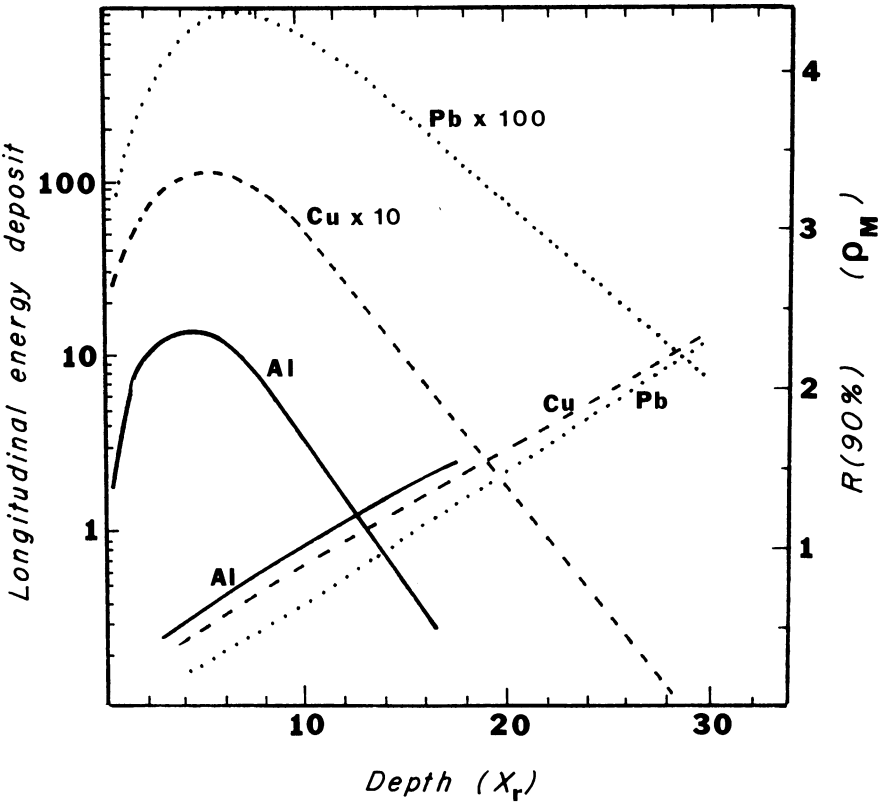
Since the processes that lead to a shower are statistical in nature, there will be fluctuations in the number of shower particles at any depth. The behavior of the particles in the first few radiation lengths is particularly important because of the amplification resulting from the later stages of the shower. For this reason, Poisson statistics do not accurately describe the fluctuations in the number of shower particles. Rossi [2] has given an informative illustration of this. First consider the probability that an incident photon will convert. On the average, photons convert after traversing a distance $t_{av} = 1.3$ radiation lengths. We know that photon con-

Downloaded from https://www.cambridge.org/core. UNIVERSIDAD AUTONOMA METROPOLITANA, on 15 Nov 2026 at 20:24:52, subject to the Cambridge Core terms of use, available at https://www.cambridge.org/core/terms. https://doi.org/10.1017/9781009290098.012

version is governed by Poisson statistics. Therefore, the probability that the photon has not converted after traveling a distance $3t_{av}$ is $e^{-3} \sim 0.05$, independent of the photon energy. Thus, there is a 5% probability of finding no electrons at a depth of 3.9 radiation lengths into the shower. However, we see from Fig. 11.2 that for a 10-GeV shower at a depth of 3.9 radiation lengths, there are on the average about 50 electrons in the shower. If the fluctuations in the number of electrons were also governed by Poisson statistics, the probability of finding no electrons would be $e^{-50} \ll 0.05$. This shows that the fluctuations observed in showers greatly exceed what is expected from Poisson statistics.

Measurements [6] of the fluctuations in the number of shower particles

Figure 11.3 Longitudinal development of electromagnetic showers in different materials. Right scale shows radii for 90% shower containment. (C. Fabjan and T. Ludlam, adapted with permission from the Annual Review of Nuclear and Particle Science, Vol. 32, © 1982 by Annual Reviews, Inc.)



Downloaded from https://www.cambridge.org/core. UNIVERSIDAD AUTONOMA METROPOLITANA, on 15 Nov 2026 at 20:24:52, subject to the Cambridge Core terms of use, available at https://www.cambridge.org/core/terms. https://doi.org/10.1017/9781009290098.012

versus the longitudinal depth in the shower show that the spread in the distributions falls to a minimum at t_{max} and then increases again as the number of particles in the shower begins to decrease. For Poisson statistics $\sigma_N/N = N^{-1/2}$. The measured fluctuations are much larger. The relative fluctuations in electron number decreases as the energy is increased.

According to Eq. 11.7, we can obtain a crude measurement of E_0 by counting the number of particles in the shower whose energy exceeds some value. A more accurate measurement comes from measuring the total ionization produced, which should be proportional to the total charged track length. The fluctuations σ_L/L of this quantity are smaller than that of the number distribution and are found to decrease inversely with depth into the shower [6].

11.2 Electromagnetic shower detectors

The shower phenomenon is utilized in electromagnetic shower detectors to detect high energy electrons and photons. Once they are properly calibrated, these devices also measure the energy of the shower and hence that of the incident particle. Detectors may consist of either a homogeneous absorber or a sandwich structure that periodically samples the energy loss. Homogeneous detectors include NaI and bismuth germanate (BGO) scintillators, scintillating glass, lead-glass blocks, thallium-doped heavy liquid counters, and liquid argon [1].

The most common types of electromagnetic sampling calorimeters are

1. metal–scintillator sandwich,
2. metal–liquid argon ionization chamber, and
3. metal–gaseous PWCs.

Each device consists of alternate layers of a metal radiator to enhance photon conversions and some active substance to sample the energy loss. The metal radiator is usually made of lead. Some typical detector arrangements are shown in Fig. 11.4. The calorimeter cells are typically arranged in either a strip or a tower arrangement [7]. In a strip structure the profile of the shower is sampled at various depths. Usually two or three profile orientations are measured. In a tower structure the calorimeter is divided into many narrow, deep units that point to the interaction region.

The calorimeter readout may be either digital or proportional. In a calorimeter with digital readout the active region is finely divided into channels, each of which can provide a yes or no signal. The energy deposition is proportional to the number of yes channels. A detector using flash tubes is an example of a digital calorimeter. In a proportional calorimeter, on the other hand, the analog signals from the active regions are summed

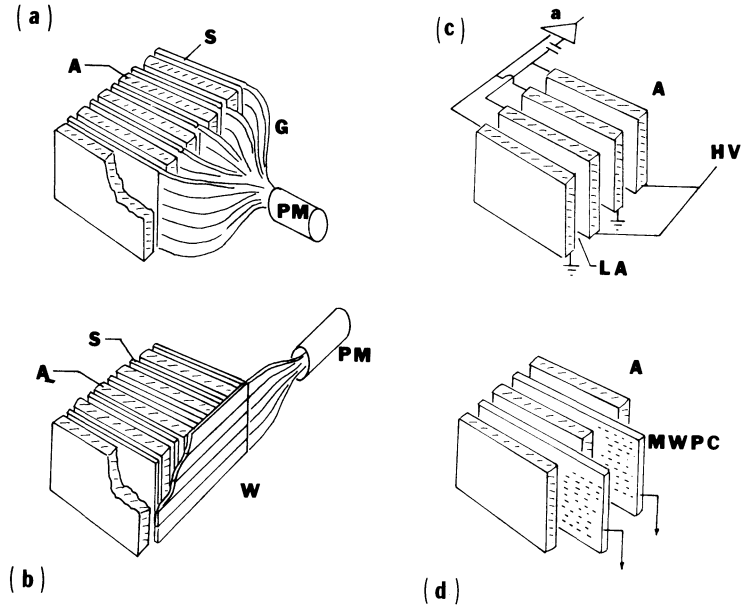
Downloaded from https://www.cambridge.org/core. UNIVERSIDAD AUTONOMA METROPOLITANA, on 15 Nov 2026 at 20:24:52, subject to the Cambridge Core terms of use, available at https://www.cambridge.org/core/terms. https://doi.org/10.1017/9781009290098.012

to produce a total signal that is proportional to the deposited energy. The lead–scintillator sandwich is an example of a proportional calorimeter.

In the scintillator devices charged particles in the shower produce light in the scintillator planes. Both solid and liquid scintillator have been used. The signal produced is usually large and very fast, making it useful in a high rate environment. Problems arise when the detector must be finely segmented or operated inside a magnetic field. The PMTs must be located in a weak field, and this may require a complicated light pipe system. Some large calorimeters have used scintillators made from polymethyl methylacrylate to reduce costs.

One solution to the readout problem illustrated in Fig. 11.4 involves passing the light from a number of scintillator layers into a bar of a second scintillator doped with a wavelength shifter such as BBQ. The emission spectrum of the POPOP in the scintillator layers is well matched to the absorption spectrum of the BBQ. The absorbed light is then reemitted isotropically at a longer wavelength. Part of the emitted light is internally

Figure 11.4 Typical readout techniques for calorimeters: (a) lead–scintillator sandwich, (b) lead–scintillator sandwich with wavelength shifter bars, (c) liquid argon ionization chamber, and (d) lead–MWPC sandwich. (C. Fabjan and T. Ludlam, adapted with permission from the Annual Review of Nuclear and Particle Science, Vol. 32, © 1982 by Annual Reviews, Inc.)



Downloaded from https://www.cambridge.org/core. UNIVERSIDAD AUTONOMA METROPOLITANA, on 15 Nov 2026 at 20:24:52, subject to the Cambridge Core terms of use, available at https://www.cambridge.org/core/terms. https://doi.org/10.1017/9781009290098.012

reflected to the PMT. This scheme allows a simpler construction with a minimum amount of dead space.

The signal from the PMT is usually fed into an ADC, which gives an output proportional to the area under the PMT signal. The time stability of the PMT gain can be checked by monitoring with a built-in LED flasher. The energy scale can be calibrated by measuring the response of the device to a muon or other minimum ionizing particle.

A liquid argon calorimeter consists of a series of metal plates immersed in liquid argon. A typical plate separation is 3 mm. The plates are maintained at a positive high voltage so that electrons produced in the liquid argon are collected at the plates. Since there is no charge multiplication, the collected charge is quite small (~ 0.6 pC/GeV), and the detector requires a preamplifier and associated electronics for each channel. It is important that the detector be free of any electronegative gases. The chamber must be operated at liquid argon temperatures (80 K) and thus requires a cryogenic system. The detector is relatively slow. The TASSO liquid argon calorimeter takes ~ 900 ns to give a pretrigger signal [8]. On the other hand, it is stable, is not adversely affected by the presence of a magnetic field, and is easily segmented. The detector has uniform sensitivity, and it is possible to make a highly accurate charge calibration.

The gaseous PWC detectors are cheaper than the other types of detectors discussed previously and can operate satisfactorily in a magnetic field. With 2-dimensional readout they can also give the correlation between the projections of the shower. This is especially important for resolving ambiguities in multishower events. Disadvantages of the PWC detectors include worse energy resolution, slow response, and lower density than the other calorimeters.

Calorimeters are widely used in particle physics experiments, particularly at the large spectrometers [1, 8]. Characteristics of some representative electromagnetic calorimeters are listed in Table 11.1.

Improved resolution has been observed with MWPCs operating in the Geiger, limited streamer, and saturated avalanche modes. Atac et al. [9] studied the response of a PWC calorimeter operating in the saturated avalanche regime to positrons with energy up to 17.5 GeV. The calorimeter consisted of 34 units, each containing a 2.8-mm-thick lead plate and a proportional chamber plane with anode wires in 9.5×9.5-mm cells. The counters used a 49.3% Ar/49.3% ethane/1.4% ethanol gas mixture. The rate of growth of the proportional chamber gain decreases continuously in the regime between proportional and streamer operation. With the high voltage set for operations in the region between these regimes, the gain is

Downloaded from https://www.cambridge.org/core. UNIVERSIDAD AUTONOMA METROPOLITANA, on 15 Nov 2026 at 20:24:52, subject to the Cambridge Core terms of use, available at https://www.cambridge.org/core/terms. https://doi.org/10.1017/9781009290098.012

sufficiently high so that the calorimeter may be operated without amplifiers between the anode wires and the ADCs in the readout electronics. In addition, there is a greater concentration of primary ionization, and the tail of the Landau distribution is greatly suppressed. As a result, the calorimeter has good linearity, good energy resolution ($\sigma/E \sim 16\%/\sqrt{E}$), and no measurable systematic effects.

The shower that actually develops in the detector depends on the incident particle type, the incident particle energy, the incident particle angle of incidence, and the spatial distribution and nature of the radiator and active layers. The response of a given detector to two identical incident particles will differ because of statistical fluctuations in the shower development. However, a properly designed detector should be capable of returning a signal that is proportional to the energy of the incident particle. The energy spectra of electrons of various energies in a liquid argon calorimeter is shown in Fig. 11.5. We see that the observed energy grows with incident electron energy [10]. The widths of the distributions do not increase linearly, so the energy resolution improves with E. We expect the response of the detector to be linear if all the energy is absorbed in the device.

Table 11.1. *Examples of electromagnetic calorimeters*

Detector	Absorber thickness (mm)	Sensitive material thickness[a] (mm)	Total depth (radlens)	σ/E $(\%/\sqrt{E})$
ARGUS	1 Pb	5 Sc	12.5	8
CELLO	1.2 Pb	3.6 LA	20	13
MARK II	2 Pb	3 LA	15	13
MARK III	2.8 Pb	12.7 PWC	12	18
Tagged γ	1.6 Pb	12.7 LSc	19	12
TASSO	2 Pb	5 LA	14	11
UA-1	3 Pb	2 Sc	26	15
AFS	1.6 U	2 × 2.5 Sc	19.5	11
UA-2	3.5 Pb	4 Sc	17	14

[a] Abbreviations: Sc, plastic scintillator; LSc, liquid scintillator; LA, liquid argon.
Source: A. Drescher et al., Nuc. Instr. Meth. 205: 125, 1983 (ARGUS); V. Bharadwaj et al., Nuc. Instr. Meth. 155: 411, 1978 (tagged γ); S. Wu, Phys. Rep. 107: 59, 1984; W. Toki et al., Nuc. Instr. Meth. 219: 479, 1984 (Mark III); R. Carosi et al., Nuc. Instr. Meth. 219: 311, 1984 (AFS); A. Beer et al., Nuc. Instr. Meth. 224: 360, 1984 (UA-2).

Downloaded from https://www.cambridge.org/core. UNIVERSIDAD AUTONOMA METROPOLITANA, on 15 Nov 2026 at 20:24:52, subject to the Cambridge Core terms of use, available at https://www.cambridge.org/core/terms. https://doi.org/10.1017/9781009290098.012

The development of the shower with depth in a liquid argon detector is shown in Fig. 11.6. We see that a lower energy electron deposits most of its energy in the early layers [11]. The 4-GeV/c electrons deposit most of their energy in the middle of the detector. The lateral spread of the shower is primarily caused by multiple scattering and is independent of the incident energy over this energy interval.

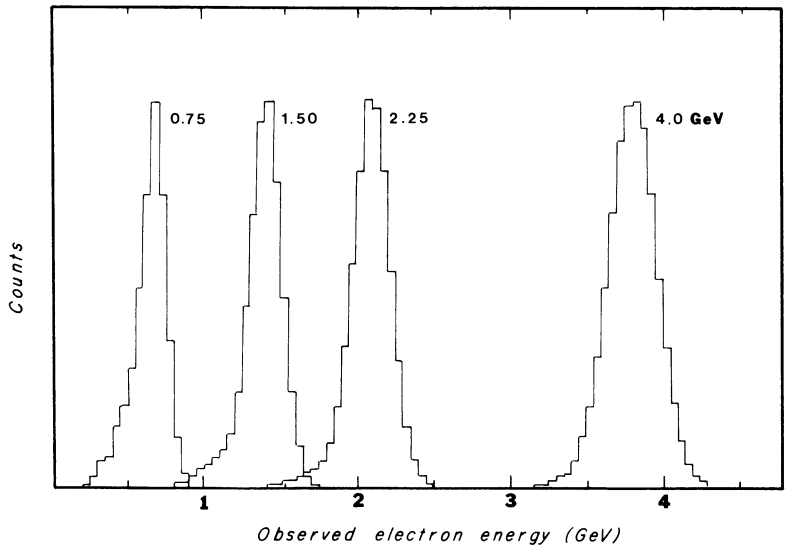
The final signal from any detector is the number of electrons that are registered in the electronic circuits. The resolution of the device for detecting an incident particle of energy E_0 is determined by fluctuations in the number N of these electrons. These fluctuations can arise from

1. the actual energy deposited in the active layers of the detector (sampling fluctuations),
2. leakage of energy out of the calorimeter,
3. noise in the active layers,
4. photocathode statistics or gain variations,
5. electronic noise, and
6. more than one event within the time resolution (pileup).

If these fluctuations follow a Poisson distribution, the standard deviation is $\sigma = \sqrt{N}$, and the resolution is

$$\sigma(N)/N = 1/\sqrt{N} \tag{11.13}$$

Figure 11.5 Observed electron energy distributions in a liquid argon calorimeter. The number by each curve gives the incident electron energy. (After J. Cobb et al., Nuc. Instr. Meth. 158: 93, 1979.)



Downloaded from https://www.cambridge.org/core. UNIVERSIDAD AUTONOMA METROPOLITANA, on 15 Nov 2026 at 20:24:52, subject to the Cambridge Core terms of use, available at https://www.cambridge.org/core/terms. https://doi.org/10.1017/9781009290098.012

The major contribution to the energy resolution of electromagnetic calorimeters is usually sampling fluctuations.

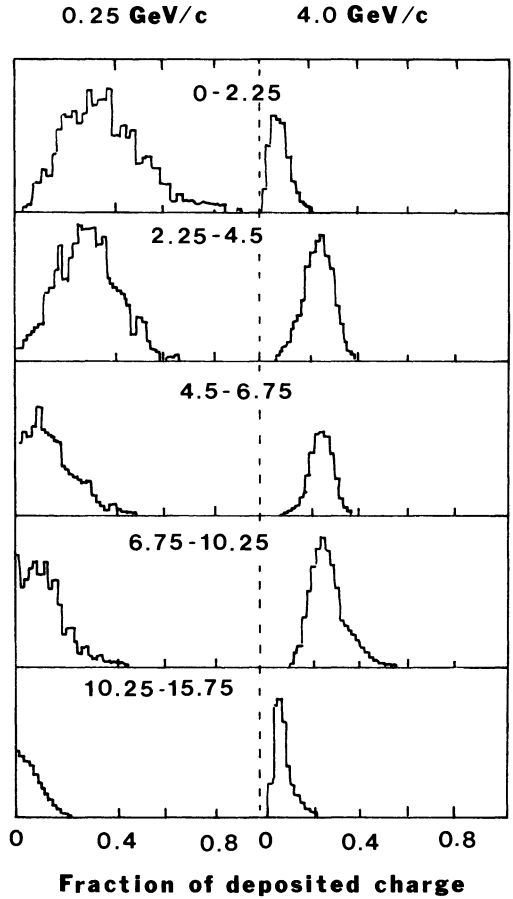
It is instructive to expand the variance of the energy distribution into a power series in E,

$$\sigma^2(E) = \sigma_0^2 + \sigma_1^2 E + \sigma_2^2 E^2 + \cdots$$

Dividing by E^2, we obtain an expansion of the energy resolution [12].

$$\left(\frac{\sigma(E)}{E}\right)^2 = \frac{\sigma_0^2}{E^2} + \frac{\sigma_1^2}{E} + \sigma_2^2 + \cdots \tag{11.14}$$

Figure 11.6 Shower profiles at five sampling depths in a liquid argon calorimeter. The left-hand curves are for a low energy electron, while the right-hand curves are for a higher energy electron. The numbers associated with each set of curves is the range of sampling depths in radiation lengths. (After D. Hitlin et al., Nuc. Instr. Meth. 137: 225, 1976.)



Downloaded from https://www.cambridge.org/core. UNIVERSIDAD AUTONOMA METROPOLITANA, on 15 Nov 2026 at 20:24:52, subject to the Cambridge Core terms of use, available at https://www.cambridge.org/core/terms. https://doi.org/10.1017/9781009290098.012

The constant σ_0 represents contributions to the resolution that are only important at low energy, primarily the ADC pedestal widths. The σ_1 term is usually dominant. Any process governed by Poisson statistics will contribute to this term. These include fluctuations in energy loss (sampling) and fluctuations in the number of photoelectrons released at the face of a PMT. Contributions to σ_2 affect the resolution curve as a whole. Hence they include calibration errors.

The signals from individual scintillator layers in a lead–scintillator detector fall off roughly like $1/\sqrt{N}$, but with a coefficient larger than the 1.0 expected from Poisson statistics [4]. The signal from the sum of all the layers more closely approximates Poisson statistics for large signals. If the detector response is linear with incident energy, the resolution should improve like $1/\sqrt{E}$.

The resolution also depends on the frequency of sampling in the detector. Fluctuations in measurements of the number of particles in the shower at any depth should go like

$$\sigma/E = 1/\sqrt{N_e} = \sqrt{\Delta E/E}$$

where N_e is the average number of sampled electrons, and ΔE is the average energy loss of electrons per sampling layer. Then

$$\Delta E \simeq E_c \, \Delta x / X_{rad} = E_c t_s$$

where t_s is the sampling thickness measured in radiation lengths. It follows that

$$\sigma/E = k\sqrt{t_s/E} \tag{11.15}$$

where k is a constant. This is roughly confirmed by the data [13]. If t_s is reduced below 0.1, the width falls off faster than $t_s^{1/2}$ due to the increased probability of detecting low energy particles in the shower [11].

The leakage of energy out the sides or end of the detector adversely affects its resolution. Leakage can be effectively studied by adding modules to the shower detector and watching the improvement in the energy resolution. In general, leakage out the end of the calorimeter is more harmful than leakage out the sides [5].

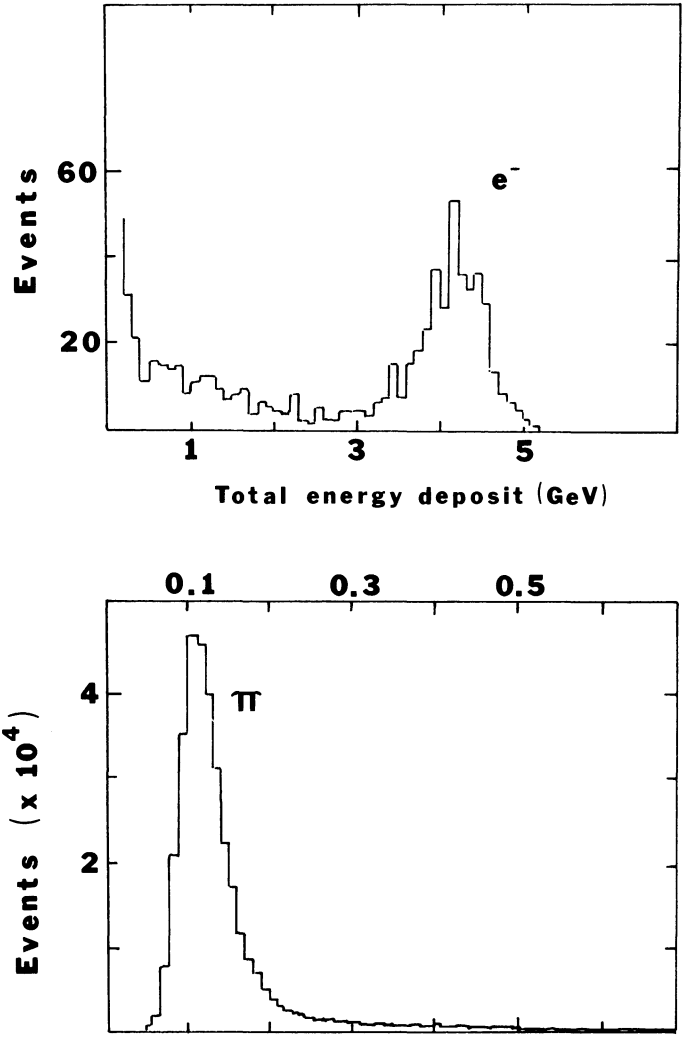
The primary reason for the worse energy resolution in PWC calorimeters is that they are subject to additional fluctuations, which are more important in gases than in liquids or solids [5]. These include fluctuations from the asymmetric Landau-like energy deposition and path length fluctuations due to low energy electrons.

Another important feature of a detector is hadron rejection. It may be necessary to detect electrons in a beam with a large pion background. In this case it is necessary to exploit the different characteristics of hadronic

Downloaded from https://www.cambridge.org/core. UNIVERSIDAD AUTONOMA METROPOLITANA, on 15 Nov 2026 at 20:24:52, subject to the Cambridge Core terms of use, available at https://www.cambridge.org/core/terms. https://doi.org/10.1017/9781009290098.012

and electromagnetic showers. The principal difference is the amount of deposited energy. Figure 11.7 shows the total energy deposited in a lead–scintillator detector by 4-GeV/c electrons and pions [14]. The electron distribution is peaked at the beam energy, showing that all its energy was contained in the calorimeter. The low energy tail results from pion contamination in the beam. The pion distribution shows a peak correspond-

Figure 11.7 Deposited energy spectrum of electrons and pions in a lead–scintillator calorimeter. Note the different energy scales for the two curves. (After G. Abshire et al., Nuc. Instr. Meth. 164: 67, 1979.)



Downloaded from https://www.cambridge.org/core. UNIVERSIDAD AUTONOMA METROPOLITANA, on 15 Nov 2026 at 20:24:52, subject to the Cambridge Core terms of use, available at https://www.cambridge.org/core/terms. https://doi.org/10.1017/9781009290098.012

ing to minimum ionizing particles that passed straight through the detector. The tail of the pion distribution extends all the way to the full beam energy, corresponding to events where the beam pion interacted and produced a π^0, which then underwent an electromagnetic decay.

Further small improvements in the hadron rejection may be made from cuts on the fraction of the total energy deposited in a given longitudinal or lateral segment of the detector. We will discuss this further in the next section. It should be noted that improvement of the hadron rejection may require a loss of energy resolution or electromagnetic detection efficiency. Thus, the various parameters have to be optimized for the particular experiment under consideration.

11.3 Hadronic shower detectors

Sampling detectors for showers initiated by hadrons are similar in construction to the electromagnetic sampling detectors. Basically the problem of hadron rejection in the electromagnetic detector becomes one of hadron optimization in the hadronic detector. In this section we will further emphasize the differences in the development of the two types of showers.

The physical processes that cause the propagation of a hadron shower are considerably different from the processes in electromagnetic showers. About half the incident hadron energy is passed on to additional fast secondaries [1]. The remainder is consumed in multiparticle production of slow pions and in other processes. A typical secondary hadron is produced with a transverse momentum of ~ 350 MeV/c, so that hadronic showers tend to be more spread out laterally than electromagnetic ones.

Table 11.2 shows the results of a calculation by Gabriel and Schmidt of the most important processes involved in the loss of energy of a 10-GeV proton in iron [15]. We see that most of the energy is dissipated by the ionization losses of scattered secondary protons. The second largest loss arises from the production of π^0's from nuclear interactions. These decay immediately into two photons and thus give rise to an electromagnetic shower within the hadronic one. The third largest loss is due to the binding energy used to break up nuclei and from the production of neutrinos.

Sophisticated Monte Carlo codes that simulate high energy hadronic showers are very useful in calorimeter design. The codes take into account relevant processes such as energy loss, particle decay, scattering, Fermi motion, neutron absorption, noise, and so on. The programs can be checked against measured low energy shower characteristics and then used to predict the expected shower behavior at high energy. The Monte

Downloaded from https://www.cambridge.org/core. UNIVERSIDAD AUTONOMA METROPOLITANA, on 15 Nov 2026 at 20:24:52, subject to the Cambridge Core terms of use, available at https://www.cambridge.org/core/terms. https://doi.org/10.1017/9781009290098.012

Carlo program of Gabriel et al. [16] predicts that the fraction of energy going into electromagnetic processes increases with increasing energy. As a result, fluctuations due to binding energy losses decrease, and the resolution should improve faster than extrapolations of low energy measurements. An overall fit to experimental and Monte Carlo data between 1 and 250 GeV gives

$$\frac{\sigma(E)}{\mathrm{E}} = \frac{33.4\%}{\sqrt{E}} + 5.07\%$$

where E is in GeV.

The longitudinal development of hadronic showers scales with the nuclear absorption (or interaction) length

$$\lambda = A/N_{\mathrm{A}}\sigma_{\mathrm{abs}} \tag{11.16}$$

where σ_{abs} is the absorption cross section discussed in Chapter 3. Figure 11.8 shows hadron-induced showers in four different materials. The lateral shower development does not scale with λ [1].

We saw in Section 2 that the electromagnetic and hadronic showers could be distinguished by the amount of energy deposition. Another important characteristic of a hadronic shower is that it takes longer to develop than an electromagnetic one [17]. This can be seen by comparing the number of particles present versus depth for pion- and electron-initiated showers. Long tails are present in the pion distributions. As a consequence, hadronic shower detectors must be deeper than electromagnetic

Table 11.2. *Average fractional energy deposition for a 10-GeV proton in an iron/liquid argon calorimeter*

Process	Percent of total
Secondary proton ionization	31.6
Electromagnetic cascade	21.0
Nuclear binding energy plus neutrino energy	20.6
Secondary $\pi^{\pm}$ ionization	8.2
Neutrons with $E > 10$ MeV	4.9
Neutrons with $E < 10$ MeV	3.9
Residual nuclear excitation energy	3.7
$Z > 1$ ionization	2.4
Primary proton ionization	2.3
Other	1.4

Source: T. Gabriel and W. Schmidt, Oak Ridge National Laboratory report, ORNL/TM-5105, 1975.

Downloaded from https://www.cambridge.org/core. UNIVERSIDAD AUTONOMA METROPOLITANA, on 15 Nov 2026 at 20:24:52, subject to the Cambridge Core terms of use, available at https://www.cambridge.org/core/terms. https://doi.org/10.1017/9781009290098.012

detectors of the same type to completely contain the shower. The mean depth of the hadronic shower energy deposition may be parameterized as [18]

$$\lambda_{\max} = 0.90 + 0.36 \ln E \tag{11.17}$$

where $\lambda_{\max}$ is in interaction lengths and the energy is in GeV.

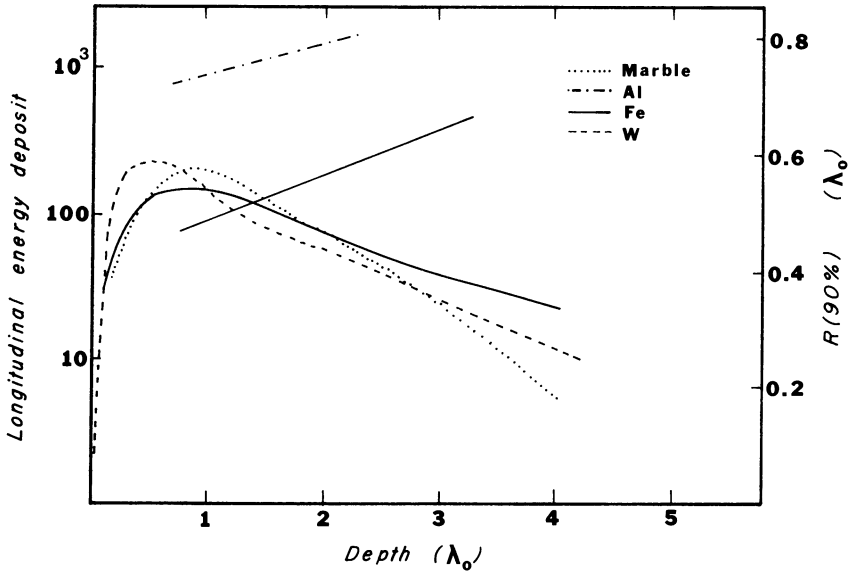
Next let us consider the integral energy deposition. Define L to be the thickness of absorber beyond which only 10% of the energy remains. Figure 11.9 shows the total deposited energy as a function of the depth in the shower. We see that up to 40 GeV essentially all the shower energy is contained in the first five interaction lengths. The data can be parameterized as [18]

$$L = -1.26 + 1.74 \ln E \tag{11.18}$$

where L is in interaction length and E is in GeV.

For finely segmented calorimeters the width of the shower can be defined in terms of the number of detector elements in which the deposited energy exceeds some minimum cutoff value. The shower grows wider as it develops due to large angle nuclear processes and multiple scattering. If

Figure 11.8 Longitudinal development of hadronic showers in different materials. Right scale shows radii for 90% shower containment. Distances are measured in absorption lengths. (C. Fabjan and T. Ludlam, adapted with permission from the Annual Review of Nuclear and Particle Science, Vol. 32, © 1982 by Annual Reviews, Inc.)



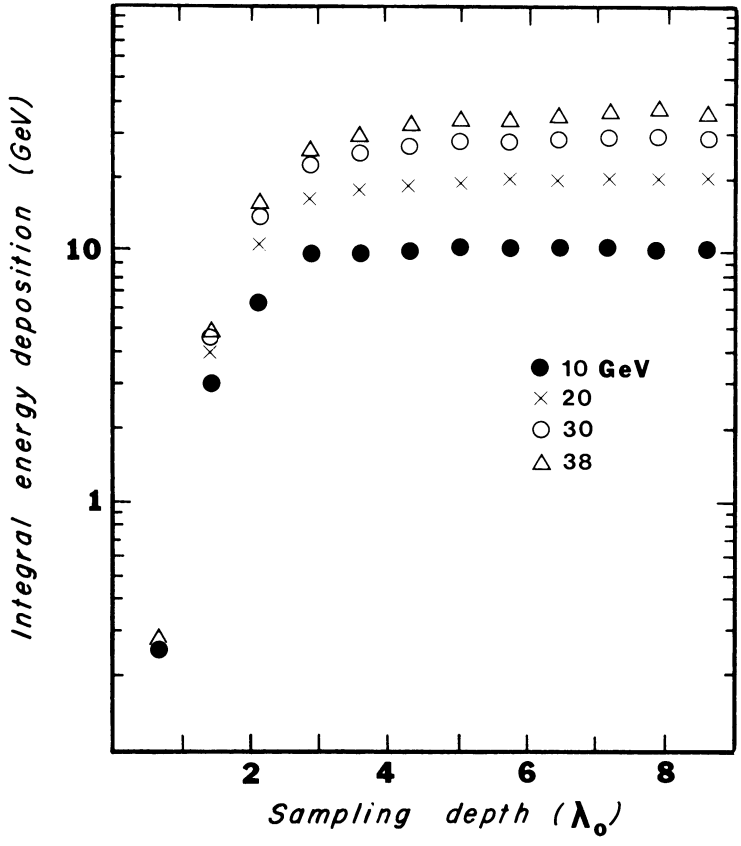
Downloaded from https://www.cambridge.org/core. UNIVERSIDAD AUTONOMA METROPOLITANA, on 15 Nov 2026 at 20:24:52, subject to the Cambridge Core terms of use, available at https://www.cambridge.org/core/terms. https://doi.org/10.1017/9781009290098.012

only nuclear processes were involved, we would expect the shower width to steadily increase until the energy of the shower particles falls below the cutoff, at which point the shower would peter out. Actually the width of the shower grows at first and then contracts. This can be seen in Figure 11.10, where the shower profiles in an iron–liquid argon calorimeter are plotted versus the depth in the shower. The narrower profiles deep in the shower are believed to be due to late developing electromagnetic processes, which tend to be produced at small angles. The shower envelope can be defined to be the width that contains 99% of the shower energy. The width of the envelope increases slowly with energy [18]

$$W(E) = -17.3 + 14.3 \ln E \tag{11.19}$$

where the width is in centimeters and the energy is in GeV.

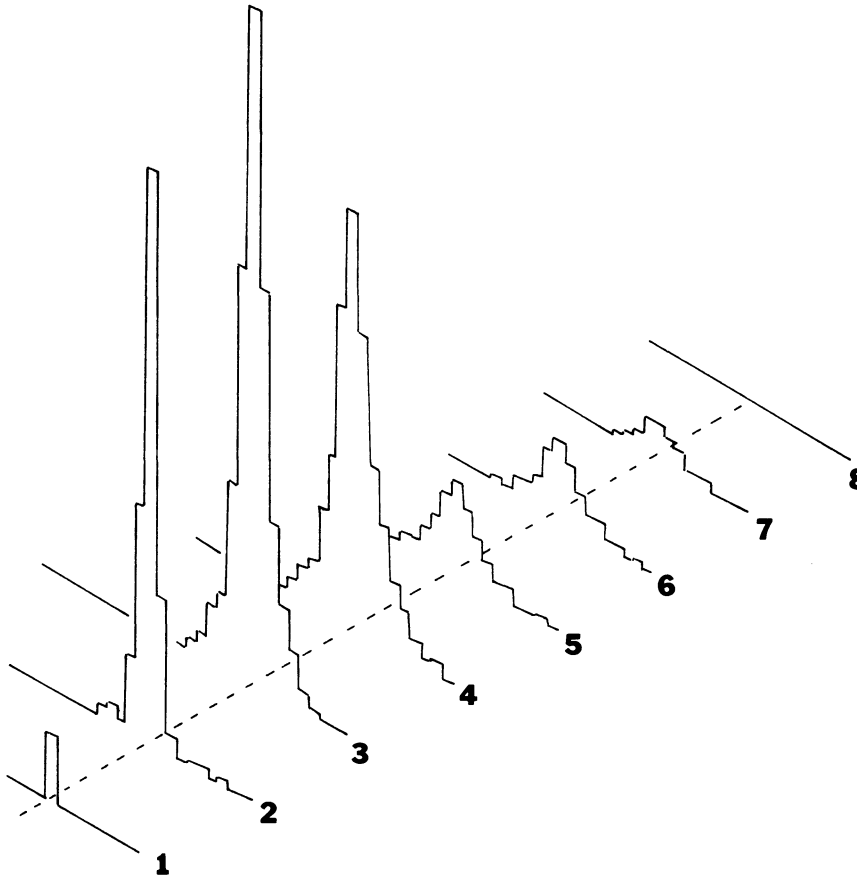
Figure 11.9 Integral energy deposition versus total sampling depth for hadronic showers. (After A. Sessoms et al., Nuc. Instr. Meth. 161: 371, 1979.)



Downloaded from https://www.cambridge.org/core. UNIVERSIDAD AUTONOMA METROPOLITANA, on 15 Nov 2026 at 20:24:52, subject to the Cambridge Core terms of use, available at https://www.cambridge.org/core/terms. https://doi.org/10.1017/9781009290098.012

Some examples of large hadronic calorimeters are listed in Table 11.3. The metal radiators most often used for hadron calorimeters are iron and lead. In general, one wants a high density since the shower depth is roughly inversely proportional to ρ. The energy resolution improves with the use of uranium plates [15]. The reason for this seems to be related to the conversion of incident energy into binding energy in nuclear interactions. This energy is ordinarily not detected. However when using uranium absorbers, some fraction of the shower energy results in the production of low energy neutrons. These neutrons can induce fission in ^{238}U, compensating for some of the lost energy through the release of fission

Figure 11.10 Transverse shower profiles at various depths in a hadronic shower. The showers originated from the interaction of a 20-GeV hadron in layer 2. (After A. Sessoms et al., Nuc. Instr. Meth. 161: 371, 1979.)



Downloaded from https://www.cambridge.org/core. UNIVERSIDAD AUTONOMA METROPOLITANA, on 15 Nov 2026 at 20:24:52, subject to the Cambridge Core terms of use, available at https://www.cambridge.org/core/terms. https://doi.org/10.1017/9781009290098.012

energy. This produces photons and electrons, which can radiate and be detected, and fast neutrons, which can scatter elastically, so that the recoil proton can be sampled.

Important aspects of calorimeter design include the solid angle coverage, operation in a magnetic field, rate characteristics, position and angular resolution, particle identification capability, resolving time, and energy resolution. The position and angular resolutions depend on the degree of segmentation of the active regions. Fine segmentation is necessary to reduce the ambiguity in multiparticle events or to separate nearby showers. This is particularly important for π^0 identification.

Some methods for particle identification using calorimeters are given in Table 11.4. Electron or photons can be identified depending on whether a charged or neutral particle initiates an electromagnetic shower. A neutral pion can be identified from the invariant mass of its decay photons. If momentum analysis is available, protons, neutrinos, and muons can also be identified in certain kinematic regions by comparing the visible energy in the calorimeter with the measured momentum.

In general, the energy resolution of hadron calorimeters is worse than that of electromagnetic calorimeters. Hadronic calorimeters are subject to all the fluctuations discussed in Section 2 in connection with electromagnetic calorimeters and to additional fluctuations due to nuclear interactions. The energy used for the production of neutrinos and high energy

Table 11.3. *Examples of hadronic calorimeters*

Detector	Absorber thickness (mm)	Sensitive thickness[a] (mm)	σ/E (%/$\sqrt{E}$)
AFS	6 U + 5 Cu	2.5 Sc	35
CDHS	25 Fe	5 Sc	58
CHARM	80 marble	PDT, 30 Sc	45
FNAL ν	16 Fe/sand	flashtubes	80
MAC	27 Fe	PWC	75
Tagged γ	25 Fe	Sc	70
UA-1	50 Fe	10 Sc	80
UA-2	15 Fe	5 Sc	60

[a] Sc, plastic scintillator.
Source: H. Gordon et al., Nuc. Instr. Meth. 196: 303, 1982 (AFS); H. Abramowicz et al., Nuc. Instr. Meth. 180: 429, 1981 (CDHS); M. Jonker et al., Nuc. Instr. Meth. 200: 183, 1982 (CHARM); D. Bogert et al., IEEE Trans. Nuc. Sci. NS-29: 363, 1982 (FNAL ν); A. Beer et al., Nuc. Instr. Meth. 224: 360, 1984 (UA-2); A. Astbury, Physica Scripta 23: 397, 1981.

Downloaded from https://www.cambridge.org/core. UNIVERSIDAD AUTONOMA METROPOLITANA, on 15 Nov 2026 at 20:24:52, subject to the Cambridge Core terms of use, available at https://www.cambridge.org/core/terms. https://doi.org/10.1017/9781009290098.012

muons and binding energy losses represents energy that "escapes" from the calorimeter. Fluctuations in the importance of these processes represent a major contribution to the energy resolution of hadron calorimeters. Other fluctuations considered by Fabjan et al. [15] in their study of hadronic energy resolution include saturation of the amplifier response to highly ionizing particles, the influence of dead regions on the sampling error, and detection of slow neutrons from a previous event. We show in Figure 11.11 the contributions to the standard deviation of the collected charge signal in liquid argon calorimeters. For electrons the width is almost entirely due to sampling fluctuations. On the other hand, the total width for hadrons incident upon iron plates is much larger than the width due to sampling variations. The total width with uranium plates comes closer to the sampling limit. In each case the hadronic resolution is worse than the electromagnetic one.

11.4 Neutral particle detectors

All neutral particle detectors require that the neutral particle have an interaction that results in the liberation of a charged particle somewhere within its sensitive volume. The detector then responds to the charged particle in the normal manner.

Slow neutrons can be captured by a nucleus, which then emits an alpha particle or a proton or undergoes fission. An important reaction of this type that occurs with boron nuclei is $^{10}B(n, \alpha)^7Li$, which has a cross section of 3830 barns for thermal neutrons. Boron may be used to line a

Table 11.4. *Particle identification using calorimeters*

Particle	Technique	Background
$e^{\pm}$	charged particle initiating electromagnetic shower	$\pi^{\pm}N \rightarrow \pi^0 x$
γ	neutral particle initiating electromagnetic shower	γ's from meson decays
π^0 and other vector mesons	invariant mass of $\gamma\gamma$ or decay products	
ν	compare visible energy with missing momentum	
μ	compare visible energy with momentum; range	noninteracting π
n or K_L^0	neutral particle initiating hadronic shower	

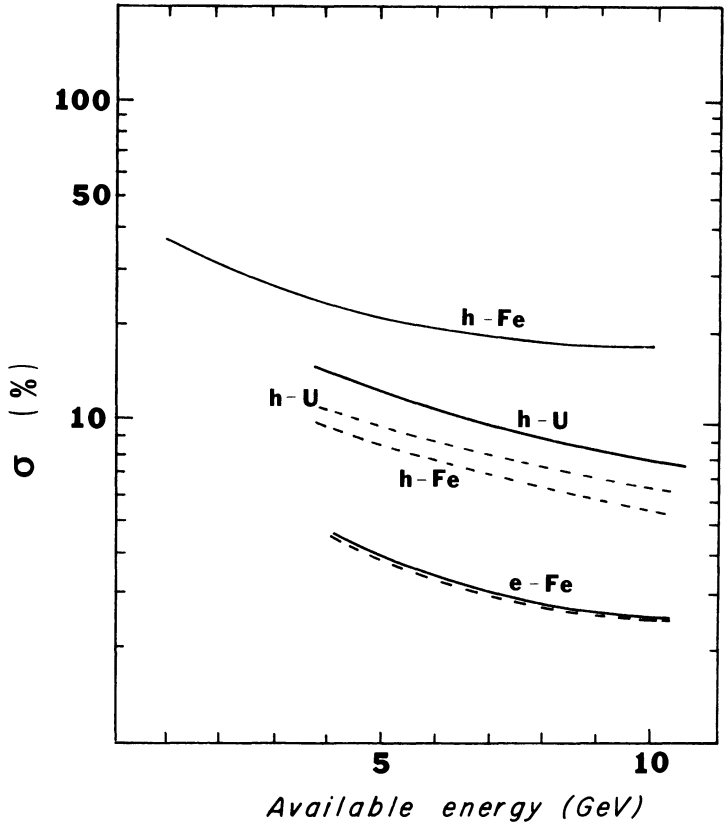
Source: C. Fabjan and T. Ludlam, Ann. Rev. Part. Sci. 32: 335, 1982.

Downloaded from https://www.cambridge.org/core. UNIVERSIDAD AUTONOMA METROPOLITANA, on 15 Nov 2026 at 20:24:52, subject to the Cambridge Core terms of use, available at https://www.cambridge.org/core/terms. https://doi.org/10.1017/9781009290098.012

chamber, or a boron-containing gas such as BF_3 may be used in a proportional counter. Coatings of ^{235}U or ^{209}Bi can fission when bombarded with slow neutrons. The fission fragments often produce a large ionization in a short range.

Fast neutrons can often be slowed down using a moderator. These are hydrogen rich compounds, such as paraffin or H_2O. Neutron capture cross sections are largest at small velocities. High energy neutrons are detected primarily by the ionization caused by the recoil proton in np elastic scattering or by a charged secondary in an inelastic reaction. They often interact in scintillator since it is hydrogen rich. However, some

Figure 11.11 Standard deviation of the collected charge distribution for different types of calorimeters as a function of the available energy. The solid curve shows the total width, the dashed curve gives the contribution from sampling fluctuations, and h refers to an incident hadron. (After C. Fabjan et al., Nuc. Instr. Meth. 141: 61, 1977.)



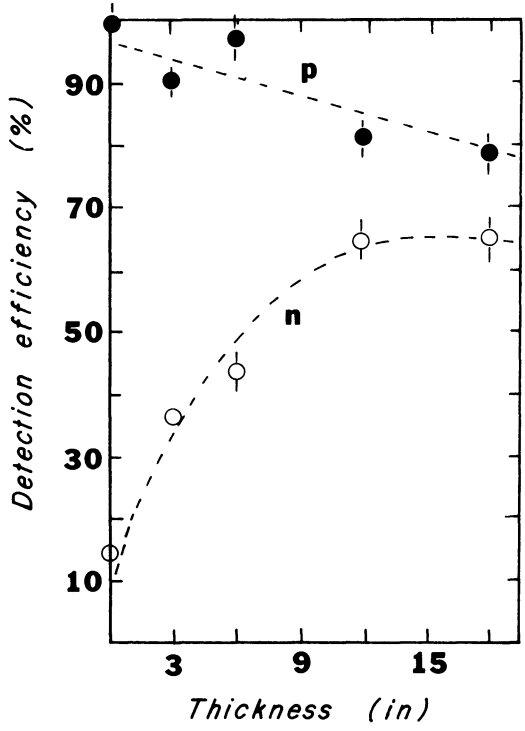
Downloaded from https://www.cambridge.org/core. UNIVERSIDAD AUTONOMA METROPOLITANA, on 15 Nov 2026 at 20:24:52, subject to the Cambridge Core terms of use, available at https://www.cambridge.org/core/terms. https://doi.org/10.1017/9781009290098.012

method, such as pulse height analysis or time of flight, may be necessary to discriminate against the detection of photons.

Steel–scintillator sampling calorimeters have been designed with good efficiency for detecting neutrons. As an example, consider the detector of Marshak and Schmuser [19], which consisted of six $\frac{1}{2}$-in.-thick layers of scintillator interspersed among sets of steel plates. The center to center separation between the scintillators was 4 in., allowing the amount of steel to be adjusted from 0 to 3 in. The measured detection efficiency, shown in Fig. 11.12, rose from 12% with no steel present to a plateau at 62% with 12 or more total inches of steel. The measured values agreed quite well with Monte Carlo calculations, based primarily on inelastic scattering. The efficiency was relatively flat over the center ± 5 in. of the scintillator and for incident neutron momenta between 2 and 5 GeV/c.

Experiments with neutrinos require very large targets because of the extremely small interaction cross section for neutrinos in matter. This

Figure 11.12 Neutron detection efficiency in a steel–scintillator neutron detector. (After M. Marshak and P. Schmuser, Nuc. Instr. Meth. 88: 77, 1970.)



Downloaded from https://www.cambridge.org/core. UNIVERSIDAD AUTONOMA METROPOLITANA, on 15 Nov 2026 at 20:24:52, subject to the Cambridge Core terms of use, available at https://www.cambridge.org/core/terms. https://doi.org/10.1017/9781009290098.012

large sensitive target volume is customarily provided by a bubble chamber or a sampling calorimeter [1, 20]. The detector must be capable of providing a large mass of material to maximize the probability that the neutrino will interact and frequent track measurements so that the neutrino interaction vertex and primary interaction products may be measured. Uniform sensitivity and the ability to resolve multiparticle events require a certain minimum degree of segmentation.

Neutrino calorimeters have been constructed using scintillators, proportional drift tubes, drift chambers, and flash tubes as the active medium. The calorimeter may be partially surrounded by scintillation counters to veto events initiated by charged beam particles or cosmic rays. However, sometimes it is convenient to use the cosmic ray muons as a calibration monitor.

References

[1] C. Fabjan and T. Ludlam, Calorimetry in high energy physics, Ann. Rev. Nucl. Part. Sci., 32: 335–89, 1982.
[2] B. Rossi, *High Energy Particles,* New York: Prentice-Hall, 1952, Chap. 5.
[3] W. Heitler, *The Quantum Theory of Radiation,* 3rd ed., Oxford: Clarendon Press, 1953.
[4] D. Muller, Electron showers of high primary energy in lead, Phys. Rev. D 5: 2677–83, 1972; comparisons of the predicted shower profiles with measurements up to 300 GeV can be found in T. Prince, The energy spectrum of cosmic ray electrons between 9 and 300 GeV, Astro. J. 227: 676–93, 1979.
[5] U. Amaldi, Fluctuations in calorimetry measurements, Physica Scripta 23: 409–24, 1981.
[6] N. Hotta, H. Munakata, M. Sakata, Y. Yamamoto, S. Dake, H. Ito, M. Miyanishi, K. Kasahara, T. Yuda, K. Mizutani, and I. Ohta, Three dimensional development of cascade showers induced by 50, 100, and 300 GeV electrons, Phys. Rev. D 22: 1–12, 1980.
[7] W. Schmidt-Parzefall, Calorimeter readout methods, Physic. Scripta 23: 425–33, 1981.
[8] A. Astbury, Calorimeter facilities, Physica Scripta 23: 397–408, 1981.
[9] M. Atac, S. Kim, M. Mishina, W. Chinowsky, R. Ely, M. Gold, J. Kadyk, P. Rowson, K. Shinsky, Y. Wang, R. Morse, M. Procario, and T. Schaad, Saturated avalance calorimeter, Nuc. Instr. Meth. 205: 113–24, 1983.
[10] J. Cobb, S. Iwata, D. Rahm, P. Rehak, I. Stumer, C. Fabjan, M. Harris, J. Lindsay, I. Mannelli, K. Nakamura, A. Nappi, W. Struczinski, W. Willis, C. Kourkoumelis, and A. Lankford, A large liquid argon shower detector for an ISR experiment, Nuc. Instr. Meth. 158: 93–110, 1979.
[11] D. Hitlin, J. Martin, C. Morehouse, G. Abrams, D. Briggs, W. Carithers, S. Cooper, R. Devoe, C. Friedberg, D. Marsh, S. Shannon, E. Vella, and J. Whitaker, Test of a lead/liquid argon electromagnetic shower detector, Nuc. Instr. Meth. 137: 225–34, 1976.
[12] H. Gordon, R. Palmer, and S. Smith, New ideas in calorimetry, Physica Scripta 23: 564–8, 1981.
[13] S. Stone, J. Poucher, R. Ehrlich, R. Poling, and E. Thorndike, Characteristics of electromagnetic shower sampling counters, Nuc. Instr. Meth. 151: 387–94, 1978.

Downloaded from https://www.cambridge.org/core. UNIVERSIDAD AUTONOMA METROPOLITANA, on 15 Nov 2026 at 20:24:52, subject to the Cambridge Core terms of use, available at https://www.cambridge.org/core/terms. https://doi.org/10.1017/9781009290098.012

[14] G. Abshire, M. Adams, C. Brown, E. Crandall, J. Goldberger, P. Grannis, J. Stekas, G. Donaldson, H. Gordon, G. Morris, and L. Cormell, Measurement of electron and pion cascades in a lead/acrylic scintillator shower detector, Nuc. Instr. Meth. 164: 67–77, 1979.
[15] C. Fabjan, W. Struczinski, W. Willis, C. Kourkoumelis, A. Lankford, and P. Rehak, Iron/liquid argon and uranium/liquid argon calorimeters for hadron energy measurement, Nuc. Instr. Meth., 141: 61–80, 1977.
[16] T. Gabriel, B. Bishop, M. Goodman, A. Sessoms, B. Eisenstein, R. Kephart, and S. Wright, A Monte Carlo simulation of an actual segmented calorimeter: a study of calorimeter performance at high energies, Nuc. Instr. Meth. 195: 461–7, 1982.
[17] D. Bollini, P. Frabetti, G. Heiman, G. Laurenti, L. Monari, and F. Navarria, Study of the structure of hadronic and electromagnetic showers with a segmented iron-scintillator calorimeter, Nuc. Instr. Meth. 171: 237–44, 1980.
[18] A. Sessoms, M. Goodman, L. Holcomb, E. Sadowski, A. Strominger, B. Eisenstein, L. Holloway, W. Wroblicka, S. Wright, and R. Kephart, The segmented calorimeter: A study of hadron shower structure, Nuc. Instr. Meth. 161: 371–82, 1979.
[19] M. Marshak and P. Schmuser, A steel/scintillator counter to detect neutrons, Nuc. Instr. Meth. 88: 77–82, 1970.
[20] B. Barish, Experimental aspects of high energy neutrino physics, Phys. Rep. 39: 279–360, 1978.

Exercises

1. A 50-GeV electron traverses a stack of iron. (a) Using the Heitler shower model, estimate the number of positrons produced after 15 cm. (b) What is the average positron energy? (c) At what depth in the stack will the number of particles in the shower reach a maximum? (d) What is the maximum number of particles present in the shower?

2. (a) Estimate the total depth of a practical 15-GeV electromagnetic calorimeter if we allow an additional $2t_{\max}$ beyond the shower maximum to minimize the probability of escaping particles. (b) How does this compare with the total depth of a 15-GeV hadron calorimeter?

3. (a) Show that the minimum opening angle of the two photons in π^0 decay is $2m_\pi/E_\pi$, where E_π is the π^0 energy. (b) Assume that the two-photon showers can be resolved if they are separated by two Moliere radii. Estimate the maximum π^0 energy that can be resolved using a practical lead–scintillator calorimeter 2 m from the interaction point.

Downloaded from https://www.cambridge.org/core. UNIVERSIDAD AUTONOMA METROPOLITANA, on 15 Nov 2026 at 20:24:52, subject to the Cambridge Core terms of use, available at https://www.cambridge.org/core/terms. https://doi.org/10.1017/9781009290098.012